From computed microtomography images to resistivity index calculations of heterogeneous carbonates using a dual-porosity pore-network approach: Influence of percolation on the electrical transport properties

D. Bauer, S. Youssef, M. Han, S. Bekri, E. Rosenberg, M. Fleury, and O. Vizika
IFP Energies nouvelles, 1 et 4 avenue Bois-Préau, 92852 Rueil-Malmaison, France
(Received 13 December 2010; published 22 July 2011)

Standard reservoir evaluations are based on Archie's law relating the average water saturation to the average electrical resistivity by $R_{\text{ind}} = S_w^{-2}$. However, especially in the case of complex heterogeneous carbonates, deviation from Archie's law is observed and generally attributed to factors affecting the percolation or disconnectedness of the different phases (wetting films, microporosity, macropores) assuring electrical conductance. Pore-network models (PNM's) in combination with high-resolution computed microtomography (μ-CT) constitute a very effective tool to investigate the influence of the geometry and topology of the porous media on the spatial distribution of the conductive phase, and therefore on the shape of the resistivity index curve. An extended version of the classical PNM applicable to dual-porosity systems is presented. It combines the classical pore-network modeling applied on the macroporous space with the macroscopic properties of the microporous phase, supposing that the two pore systems act in parallel. Three-dimensional images provide information on the connectedness of the microporous phase, which is then included in the simulations. Electrical behavior of sandstone and two carbonates presenting distinct resistivity index curves were simulated and compared to measurements. Both Archie and "non-Archie" behavior were correctly reproduced, and the curve shape was explained considering percolation of the different phases.

DOI: 10.1103/PhysRevE.84.011133 PACS number(s): 05.60.Cd, 07.05.Tp, 07.05.Rm

I. INTRODUCTION

Standard reservoir evaluations for the estimation of initial oil in place are based on Archie's laws relating water saturation (S_w) to electrical resistivity R_t. One of the steps in the estimation procedure is the determination of the resistivity index curve ($R_{\text{ind}} = R_t/R_0$, where R_0 is the resistivity at full saturation) relating R_{ind} to S_w. Conventionally, in the absence of core measurements, $R_{\text{ind}} = S_w^{-n}$ and the saturation exponent n is taken equal to 2 based on historical measurements performed on sandstones [1,2]. However, in some cases the saturation exponent n can largely deviate from 2, or become nonlinear on a log-log scale [3–6], yielding a large underestimation of oil in place, especially at low saturation. Considerable effort has been made to explain the physical reason for this variation and try to predict it from direct observations of the pore structure. However, considering a large variety of carbonate structures, it was observed in [7,8] that deviation or non-Archie behavior are not necessarily linked to bimodal structures, and that simple unimodal structure can also present strong deviation at low water saturation. In the case of unimodal structures, Han *et al.* [9,10] attributed the observed bending down on a Fontainebleau clay-free sandstone to "thick" films, whereas in [11,12] the authors explained the observed bending down behavior by microporosity lining the grains, yielding a parallel path for the current. Such an interpretation has often been used in the past for clayey sandstones [13,14]. Despite their different origins, both films and microporosity provide hydraulic continuity once the bulk conducting phase becomes disconnected. In carbonates containing microporosity, percolation arguments have been used to explain deviations from Archie's law [3,15,16]. Indeed, Archie's law relates average saturation to average resistivity with the underlying hypothesis of small local porosity and saturation changes [16], which is not the case for carbonates. Most of the studies conclude that the shape of R_{ind} curves depends on the geometrical and spatial distribution of the conductive phase, emphasizing again the percolation issue. Indeed, the shape of R_{ind} curves reflects the percolation or disconnectedness of the different water fractions (wetting films, microporosity, macropores) contributing to the electrical conductance. Montaron [17] reproduced R_{ind} curves with a large range of saturation exponents by simply introducing a so-called water connectivity index into the resistivity index equation given by percolation theories [18]. In physical terms, introducing a water connectivity index permits modeling of the wettability of the medium.

Nevertheless, it is relatively difficult to directly introduce information on the geometry and topology of the medium into percolation models. The spatial arrangement between, e.g., micropores and macropores in addition to water films strongly influences the shape of R_{ind} curves. Our approach is to combine high-resolution computed microtomography (μ-CT) images and numerical modeling to investigate R_{ind} curves as they enable us to account for the complex spatial structure as well as wetting films. Several papers in the literature treat the problem of electrical conductivity of porous structures. Generally, governing equations are directly solved in the three-dimensional (3D) pore space obtained from segmented images. For example, Bekri *et al.* [19] used finite volumes to solve for the electrical potential, whereas Knackstedt *et al.* [11] used a finite-element method to solve the Laplace partial differential equation. Han *et al.* [10] used a random-walk algorithm applied to the partially desaturated system to determine R_{ind} curves from the simulated effective diffusivity. Particles were displaced in either the film or the bulk phase. All approaches gave interesting insight into the physics of electrical conductance in partially saturated rocks. It is worthwhile, therefore, to continue these efforts and to explore, particularly in the case of dual porosity systems, the

 ©2011 American Physical Society

influence of the correlation between the rock structure and the type and number of conductive paths on R_{ind} curves. This can also be done by using a dual-porosity network approach combined with μ-CT images. The major advantage of this approach, which is described in the present paper, lies in the fact that it takes into account the essential features of the pore topology of large pores as well as the conductance of the microporous phase and of the wetting films. In particular, we will see that we can study the percolation effects of the different water fractions.

Pore-network models (PNM's) represent the pore space by a three-dimensional network of interconnected pores and throats of simple geometry (circular, elliptical, or triangular cross section), in which the effective electrical and hydraulic conductances can be determined analytically [20–22]. Although this kind of model does not describe the exact morphology of a porous medium, it is able to take into account essential features of the pore-space geometry and topology, including the converging-diverging nature of pores, the multiple connectivity of the pore space, as well as the distribution of pore sizes. PNM's are commonly used to simulate drainage and imbibition processes and to compute petrophysical properties of porous media [23–28]. Single pore-network approaches have been used extensively to calculate electrical transport properties of partially saturated porous media. A major effort was made to explain the influence of the pore topology and geometry as well as wettability alterations and saturation history on *RI* curves. In 1984, Dicker and Bemelans [29] observed the bending-down behavior at low water saturations if the presence of water films remaining along the pore wall roughness is correctly modeled. This fact has been confirmed by Sen *et al.* [16] and Zhou *et al.* [30], pointing out that in this saturation range, flow in corners becomes important and that simple bond percolation models cannot correctly represent the observed bending-down behavior. Wang and Sharma [31] and Sharma *et al.* [32] observed a strong influence of the connectivity and the aspect ratio on the saturation exponent that, in turn, strongly depends on the considered wettability. Suman and Knight [33] investigated the relation between the spatial correlation of the pore size and the saturation exponent. Man *et al.* [34,35] concluded that the slight non-Archie behavior of sandstones can be reproduced when using a realistic representation of the pore structure. Tsakiroglou and Fleury [36] included the porosity due to the fractal roughness of the pore walls. They stated that strong "non-Archie" behavior can be modeled for a certain fractal dimension of this surface roughness. This brings us to the dual network approach suitable for bimodal pore structures, considering a microporous phase acting electrically in parallel to the macroporous network. Initially proposed by Ionnidis and Chatzis [37] and extended by Bekri *et al.* [38,39], Moctezuma *et al.* [40], and Youssef *et al.* [41], this model enables the investigation of the influence of the microporous phase on the macroscopic transport. In the present work, we pursue these efforts by combining the dual network approach with μ-CT imaging. The development of computational methods to analyze the 3D structure of pore networks improved tremendously with the advent of synchrotron x-ray computed microtomography [42–46]. Recent emerging laboratory μ-CT equipment, providing resolutions of a few microns, has given a new invigoration to 3D material characterization.

The objective of the present work is to investigate the effect of pore architecture obtained from μ-CT images on electrical properties calculated with a dual-porosity pore-network model used in drainage conditions. The structure of the paper is as follows: In Sec. II, we describe the sample characteristics, including mercury injection, formation factor, and resistivity index data during drainage. Section III provides information on the image acquisition and processing. Additionally, the network and data extraction methodology is explained. Basic equations of the dual-porosity pore- network approach are given in Sec. IV. Results are then presented and discussed in Sec. V, with Sec. V A dedicated to the validation of the PNM on a monomodal sandstone sample. Then the dual-porosity PNM is applied to two distinct carbonates. A parametric study to evaluate the impact of the local heterogeneity pattern of the microporous phase is part of that section.

II. SAMPLE CHARACTERISTICS

The following samples were considered: a clay-free monomodal Fontainebleau sandstone and two carbonates (Estaillade and Lavoux limestone), characterized by a bimodal pore size distribution. The experimentally obtained petrophysical properties (permeability, K; porosity, ϕ; mercury intrusion interpretation (pore entry diameter) and resistivity index–saturation curve, $R_{\text{ind}} - S_w$; and formation factor, F_f, defined as $F_f = R_0/R_w = a\phi^{-m}$, where R_w is the resistivity of the saturating fluid, m is the cementation exponent, and a is a constant) are summarized in Fig. 1. Fontainebleau sandstone is characterized by the absence of microporous phases (clays) and the presence of a non-negligible roughness on the pore walls [scanning electron microscope (SEM) images]. The associated drainage $R_{\text{ind}} - S_w$ curves (taken from [10]) show two different regimes depending on the saturation range: the data points follow a classical power law with an exponent n close to 2 for brine saturations higher than 20%, while a bending- down behavior is observed at low S_w. As can be seen from the SEM images, both carbonates consist of macropores, micropores and a relatively dense, solid phase that might contain very small submicropores. However, samples exhibit very different electrical behaviors. Estaillade limestone contains individual microporous "red algae" grains, and the associated $R_{\text{ind}} - S_w$ curve in drainage exhibits a non-Archie behavior. The curve shows a positive deviation when the water saturation is below 40%. On the contrary, the Lavoux limestone contains an abundant microporosity, about 60% of the total porosity. The curve $R_{\text{ind}} - S_w$ follows Archie's law almost perfectly with an exponent value nearby 1.9. More information on R_{ind} measurements can be found in [8].

III. IMAGE ACQUISITION, PROCESSING, AND DATA EXTRACTION

A. Imaging setup

The μ-CT equipment is a Nanotom from PHOENIX X-Ray. Common acquisition parameters for rock analysis

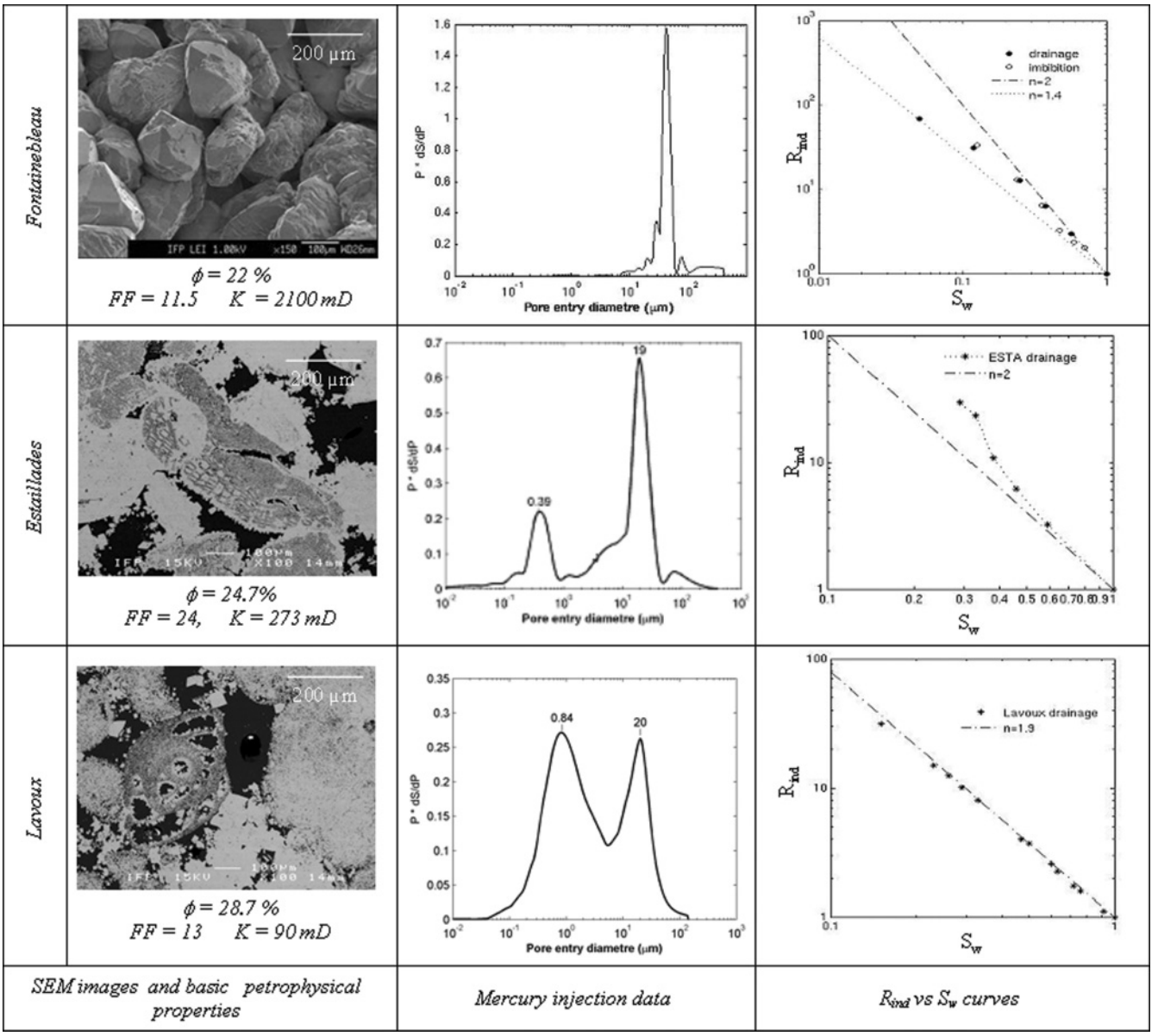

FIG. 1. Measured petrophysical properties of the studied samples.

are the following: 5-mm-diam sample, pixel size μm (corresponding to the highest possible resolution for this sample size), and 2300^2 field of view (for more details, see [47]). To optimize 3D image contrast, a sample of Estaillade limestone was imaged with three different setup conditions. Different numbers of projections (1800 and 3600) and filters (Cu and Al) were used. We clearly observed that increasing the number of projections drastically reduces noise and enhances the image contrast for a given filter without any counterpart except a longer acquisition time. The use of an aluminum filter enhances the contrast, but this gain is counterbalanced by the outbreak of ring artifacts. However, ring artifacts do not deteriorate the image quality when using a copper filter. Following these observations, a number of projections of 3600 and a 0.5-mm-thick copper filter were chosen for further acquisitions.

B. Sample imaging

Samples were imaged according to the optimal setup defined above. For each scan, a volume of 1000^3 voxels was reconstructed and converted in an 8-bit gray-level image. Figure 2 shows slices extracted from the reconstructed volumes. For the two carbonates, we can distinguish a resolved macroporosity (pore size >3 μm), the microporous phase (pore size < 3 μm, intermediate gray level), and the solid phase (bright grains).

C. Image segmentation

Image segmentation is a crucial step in image analysis. It aims to separate the different phases present in the raw image by assigning to each voxel of the image the corresponding phase depending on its gray level. We distinguish two cases:

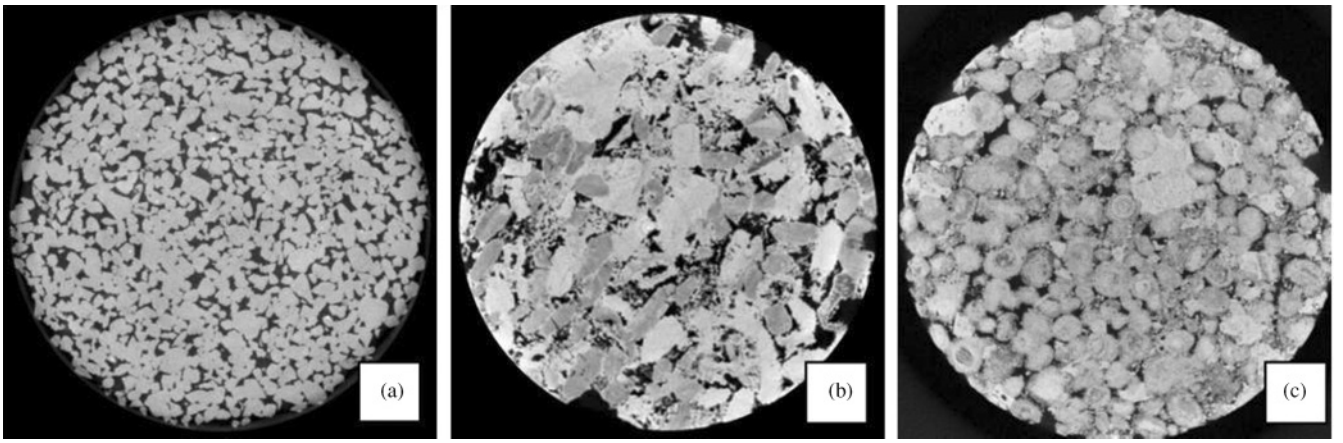

FIG. 2. X-ray density maps of Fontainebleau sandstone (a), Estaillade (b), and Lavoux limestone (c). Samples are imaged with 3-μm resolution, sample diameter 5 mm.

two-phase and three-phase segmentation. In the first case, we only consider the resolved porosity (pore size $>\mu$-CT resolution). Two-phase segmentation is well adapted to monomodal pore structures [cf. Fig. 2(a)] and is commonly done by thresholding at the minimum interpeak of the gray level histogram. Voxels belong then either to the solid or to the void space. In bimodal pore structure samples, we aim to correctly separate the solid phase, the macropores, and the microporous phase, where the limit between micro and macropores is given by the μ-CT image resolution [cf. Figs. 2(b) and 2(c)]. In this case, three-phase segmentation has to be performed.

D. Three-phase segmentation

To separate the gray levels corresponding to each phase, the images were previously filtered. The filtering operation consisted in assigning to each voxel the average gray value of its 5^3 neighbors [cf. Fig. 3(b)]. This type of filter was found to

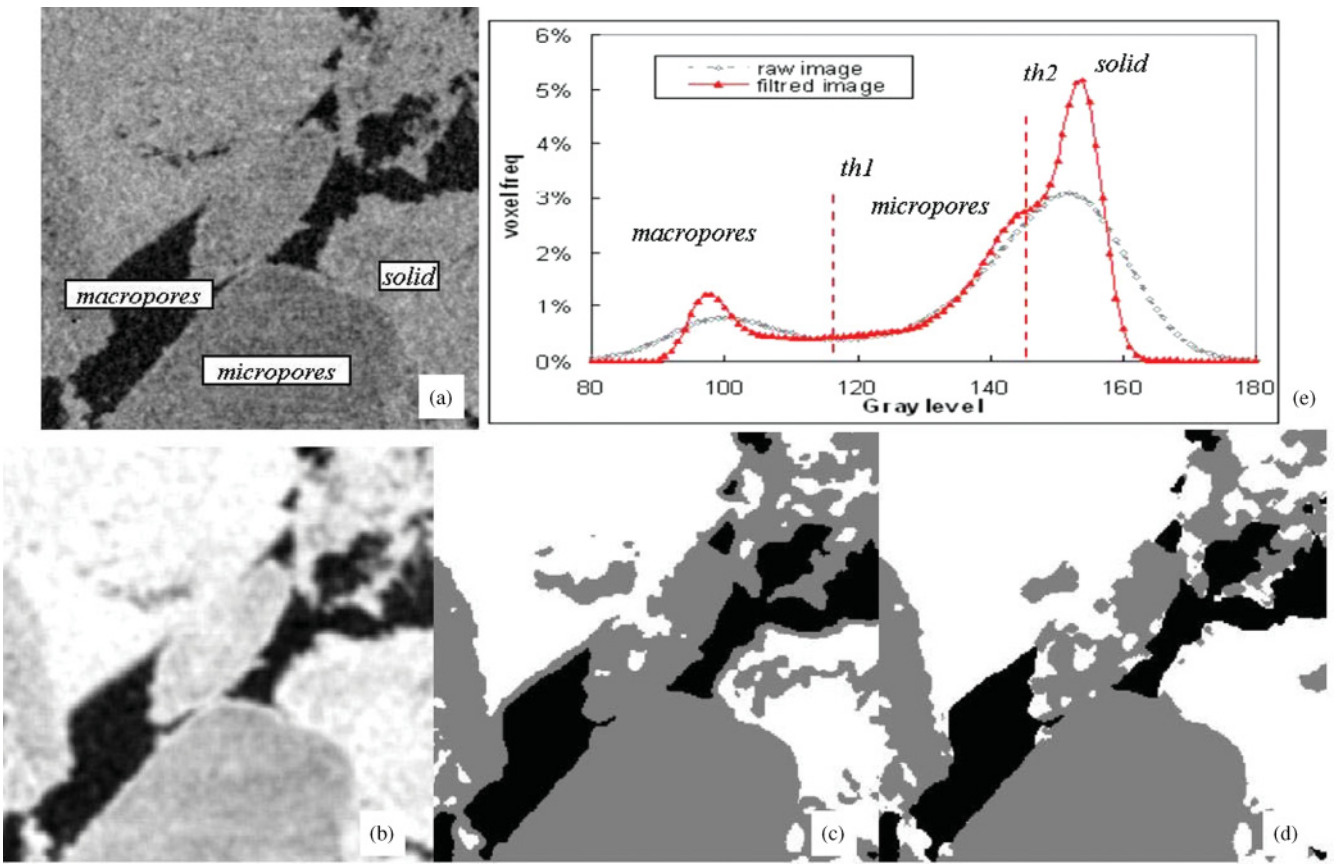

FIG. 3. (Color online) Three-phase segmentation sequence: (a) 8-bit gray-level raw image, (b) filtered image, (c) resulting composite image after applying th1 and th2, (d) final three-phase image after morphological operations, and (e) gray-level histogram.

TABLE I. Porosity of the samples and phase fraction from 3D images: image porosity (ϕ_{img}), macropore fraction (F_{ma}), microporous phase fraction (F_{mi}), porosity of the microphase (ϕ_{mi}), and fraction of the macropore surface in contact with the microporous phase (F_{surf}).

Sample ID	ϕ_{exp} (%)	ϕ_{img} (%)	F_{ma} (%)	F_{mi} (%)	ϕ_{mi} (%)	F_{surf} (%)
GdF	22.0	21.6	21.5	no.	no.	no.
EST 1	24.7	25.7	15.3	28.6	36	47
LAV 2	28.7	29.8	11.6	62.7	28	78

be a good compromise between the elimination of noise and the smoothing effect. It results in an enhanced contrast and a better separation of the gray level peaks in the histograms [cf. Fig. 3(e)]. By applying thresholds th1 and th2, a new composite image of the 3D phase distribution can be obtained [cf. Fig. 3(c)]. The resulting image still contains some artifacts due to phase transition between the void space and the solid phase (the gray level of the interface is of the same order of magnitude as that of the microporous phase). This artifact is corrected by morphological operations (growing, shrinking, and smoothing) equivalent to an isotropic dilatation [48] as shown by Fig. 3(d). Porosity can be directly deduced from the gray level histogram. According to the Beer-Lambert law, when an x-ray crosses a material, its attenuation is a function of the x-ray energies, the atomic number of the material, and its densities. The Beer-Lambert law is given by $N_t = N_i e^{\mu x}$, where N_t and N_i are the initial and final x-ray intensity, μ is the material's linear attenuation coefficient, and x is the length of the x-ray path. After reconstruction, the resulting 3D images represent the map of the local attenuation coefficients of the material. For constant energy in the photoelectric domain (energy below 200 KeV), as is the case in the present study, the linear attenuation coefficient and density are proportional for a given material. This can be expressed as $\mu = \mu_0 \rho Z^4$, where ρ is the local density of the sample, μ_0 is a scale factor for the reconstruction process, which depends on the x-ray energy and the acquisition geometry, and Z is the material atomic number.

Fontainebleau sandstones are monomineral rocks, thus their atomic number can be considered as constant in the sample. As a result, the local gray level of the images, which is proportional to the attenuation, is a linear function of the local density and hence the local porosity. If we consider that the gray level of the void space corresponds to a porosity of 1 and the gray level of the solid phase corresponds to a porosity of 0, global porosity is then obtained from the 3D image by

$$\phi_{img} = (g_s - g_m)/(g_s - g_v). \quad (1)$$

Here, g_m represents the mean gray level of the image, and g_v and g_s correspond to the gray levels of the maxima of the void and solid phase in the histogram. Porosity estimations from the images are in good agreement with the experimental ones, with slight deviations that can be attributed to local heterogeneity (cf. Table I).

E. Information extracted for simulations

1. Porosity data

The different phase fractions extracted from the composite image (reported in Table I) can be expressed as $F_{ma} = N_{ma}/N_{img}$ and $F_{mi} = N_{mi}/N_{img}$, where F_{ma}, F_{mi}, N_{ma}, N_{mi}, and N_{img} are, respectively, the resolved porosity fraction, the microporous phase fraction, the number of voxels of the resolved porosity, the number of voxels of the microporous phase, and the total number of voxels in the image. The mean porosity (ϕ_{mi}) of the microporous phase can then be deduced from

$$\phi_{mi} = (\phi_{img} - F_{ma}) / F_{mi}. \quad (2)$$

Another important parameter that can be obtained at this stage is the fraction of the surface of macropores in contact with the microporous phase (F_{surf}). To achieve this, triangulated surfaces representing the boundaries between the different phases are generated from the composite image (cf. Fig. 4). The creation of surfaces with the correct topology and optimized triangular shapes from the segmented tomographic data is carried out automatically with the help of the marching cubes algorithm [49].

F. Equivalent pore network

The pore-network extraction methodology validated on sandstones and carbonates captures the resolved pore space of the rocks to partition it into individual pore volumes separated by throat surfaces. The extraction is processed in three steps: skeletonization, pore space partitioning, and parameter calculation. The skeleton algorithm applied to the binary image is a hybrid algorithm combining thinning and distance

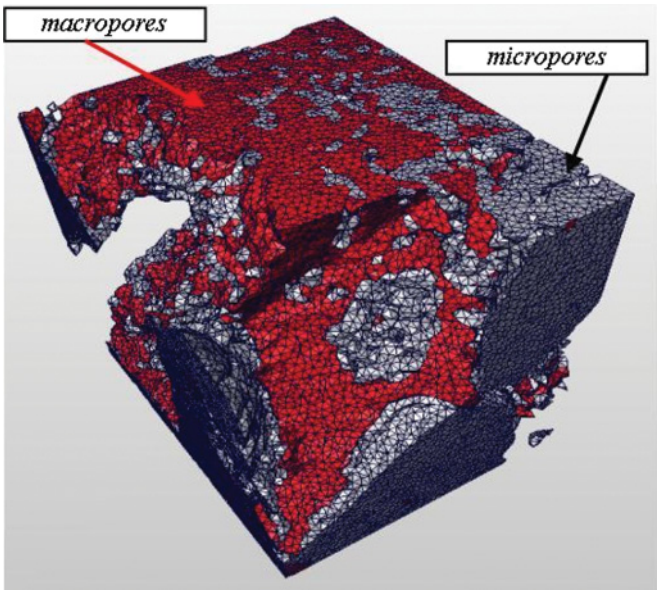

FIG. 4. (Color online) Surface model representing macropores and microporous phase of the Estaillade limestone.

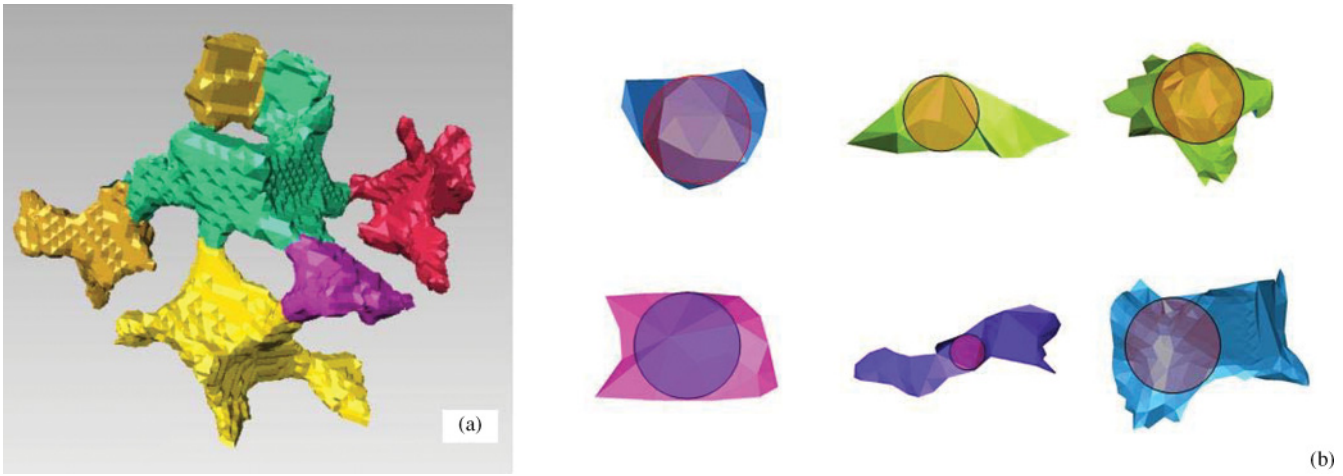

FIG. 5. (Color online) (a) Enlarged view of the partitioned volume; six pores are represented with different colors. (b) Throat surfaces and their corresponding maximal inscribed sphere.

map-based techniques called distance ordered homotopic thinning [50]. Pores are individualized and characterized by their volumes V_P^k. The pore volume intersections define the throat surfaces A_{scan}. Despite having a defined length, which will be used for the conductance calculation, throats have zero volume. Thus, the total pore volume is given by $V_P = \sum_k V_P^k$. For further information on pore-network extraction, we refer to [47]. Figure 5(a) shows an enlarged view of the partitioned volume to illustrate the quality of partitioning, while Fig. 5(b) illustrates the shape complexity of throat cross sections. The last step of the network extraction consists in attributing geometrical parameters to the pore bodies and throats that are used later for the PNM calculations.

G. Geometrical pore and throat parameters

A pore body is defined as a porous volume closed by restrictions. Its volume is measured from the partitioned 3D image of the pore space. We defined its radius as the radius of the equivalent sphere having the same volume.

Pore throats are defined as the pore restrictions given in Fig. 5(b). On the 3D images, each pore throat is characterized by its area A_{scan} and its minimum radius r_{min}. The minimum radius r_{min} corresponds to the radius of the maximal sphere inscribed in the throat cross section [cf. Fig. 5(b)]. In the PNM simulation, throats have a length that should also be determined from the images. To this end, channels of the segmented image [cf. Fig. 6(b)] can be represented by a series of elementary cylinders of variable and known radii r_i and of equal (one voxel) thickness. r_i radii are measured on the 3D image and stored as gray levels in the skeleton image, as shown in color in Fig. 6(a). The objective is then to define the length l_{ff} of an equivalent cylindrical tube of radius r_{min} having the same electrical conductance g_{eq} as the series of elementary cylinders.

The electrical fluid conductance of an elementary cylinder i is defined by

$$g_i = c\frac{r_i^2}{l_i}, \tag{3}$$

where c is a constant proportional to the bulk water conductivity. The inverse of the conductance g_{eq} of the equivalent cylindrical tube is given by

$$\frac{1}{g_{\text{eq}}} = \frac{1}{c}\frac{l_{ff}}{r_{\text{min}}^2}, \tag{4}$$

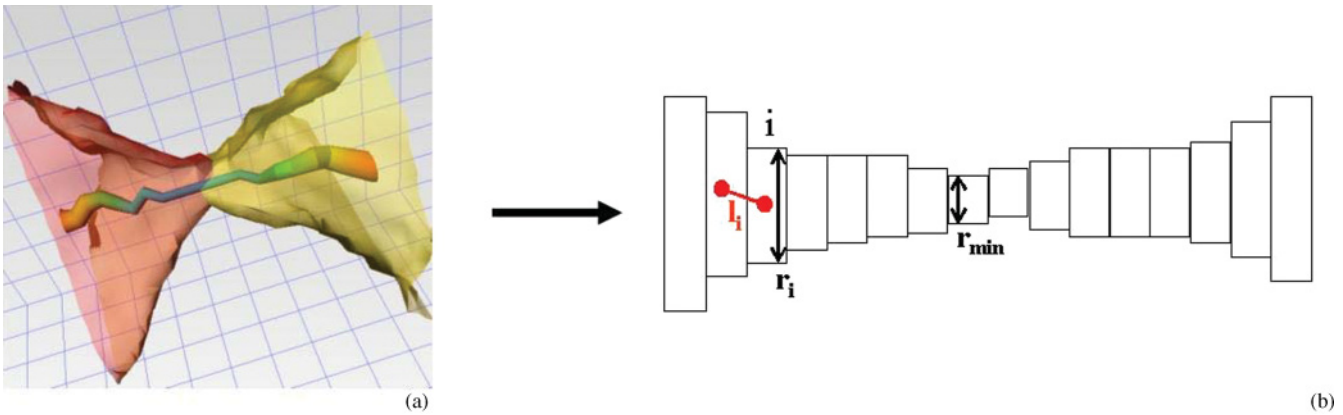

FIG. 6. (Color online) Schematic representation of a real channel connecting two pores.

which is supposed to be equal to

$$\frac{1}{g_{\text{eq}}} = \Sigma \frac{1}{g_i} \tag{5}$$

and

$$\frac{1}{g_{\text{eq}}} = \frac{1}{c} \sum_{i=1}^{n} \frac{l_i}{r_i^2}. \tag{6}$$

Thus by combining Eqs. (4) and (6), the length of the equivalent cylindrical tube with radius $r_{\min}$ becomes

$$l_{ff} = \sum_{i=1}^{n_{\max}} l_i \left(\frac{r_{\min}}{r_i} \right)^2, \tag{7}$$

where $n_{\max}$ is the number of elements in the real channel line. This length l_{ff} may be very different from the actual channel length from one pore to the other.

IV. PORE-NETWORK MODELING

In this subsection, we present the classical PNM approach commonly used for monomodal porosity rocks. Then, we explain the dual network approach suitable for bimodal pore structures.

A. Network invasion methodology

The capillary-pressure–saturation curve is obtained by simulating a quasistatic displacement. To this end, increasing pressure is applied to the injected fluid, whereas the pressure of the fluid in place is kept constant. During a quasistatic displacement, viscous pressure gradients are negligible, and the pressure of each phase is constant everywhere within the network. Expressions to evaluate the saturations in each unit element can be found elsewhere [51]. The presence of surface angularities is of high importance to model the flow of the wetting phase. Pore shapes are considered to be angular (triangular and square radius for pore throats and pore bodies, respectively), allowing the wetting phase to flow along the corners.

B. Wetting films

The area of the wetting phase occupying the corners of the pores and throats is given by [52]

$$A_w = n_c \rho^2 [\cos\theta(\cot\alpha \cos\theta - \sin\theta) + \theta + \alpha - \pi/2], \tag{8}$$

where n_c represents the number of corners, α is the half-angle of the polygon, θ is the contact angle, and ρ is the radius of the curvature of the oil-water interface, depending on the applied pressure. Thus, the wetting phase cross section decreases with increasing pressure. The ratio A_w/A_{scan} defines the surface ratio occupied by the wetting phase in the throat cross-sectional area.

C. Formation factor and resistivity index calculation

The electrical conductance of the water phase in a pore segment is given by

$$g_e = \sigma_w A_{w,s}/l_{ff}, \tag{9}$$

where $A_{w,s}$ represents the cross-sectional area occupied by the water phase (bulk: $A_{w,s} = A_{\text{scan}}$ or film: $A_{w,s} = A_w$), l_{ff} is the segment length, and σ_w is the electrical conductivity of bulk water. The calculation of the effective conductance between two neighboring pores takes into account the water phase occupancy in the different pore segments (pores and throats). The electrical current I_{ij} in each segment then becomes

$$I_{ij} = g_{e,ij}(U_i - U_j), \tag{10}$$

where U_i and U_j denote the electrical potential in the neighboring pores i and j.

D. Dual-porosity structure

The dual network model combines transport properties of the microporosity with the single pore network modeling approach applied to the interconnected macroporosity network. Both porosity types are supposed to act electrically and hydrodynamically in parallel. Thus, we consider two parallel networks, connected at the nodes, where the fluid exchange

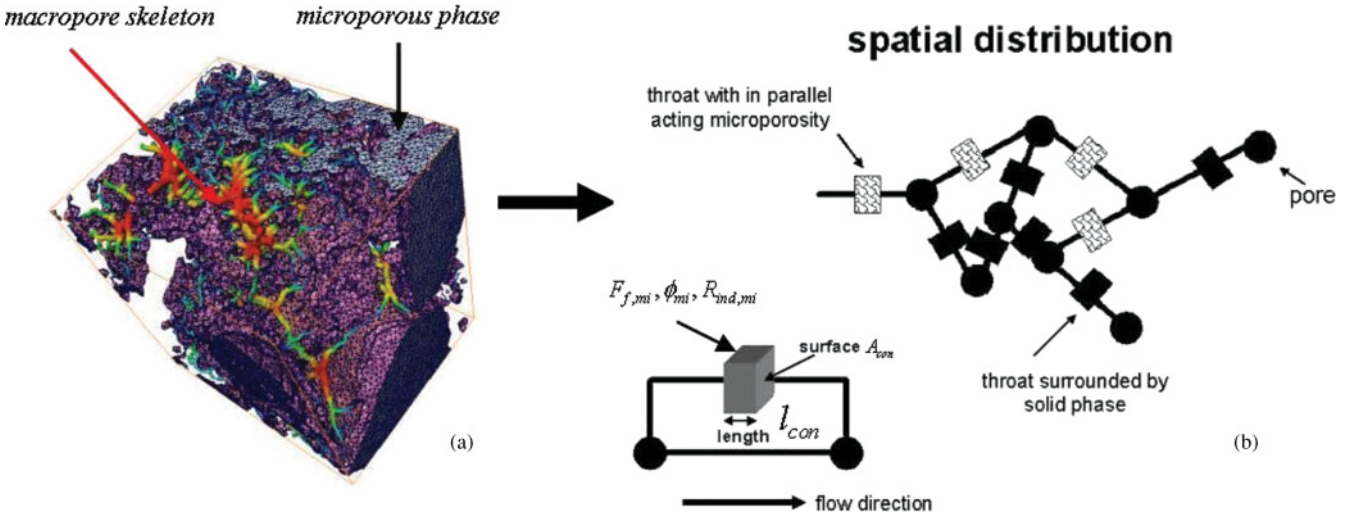

FIG. 7. (Color online) Description of the matrix surrounding the throats corresponding to the macroporosity [(a) Macropores surrounded by either microporous or solid phase, (b) corresponding microporosity distribution in the PNM].

takes place. The first one corresponds to the macropores, whereas the second one represents the macroscopic transport properties of the microporous phase (see Fig. 7). In the present work, pore-throat radii larger than the μ-CT resolution are used to build a three-dimensional interconnected network of pores and throats representing the macroporosity. Pores smaller than the μ-CT resolution are supposed to belong to the microporosity. Considering this fact, the capillary pressure P_c necessary to invade the microporous phase is always higher than the one required for the invasion of the macropores. Thus, during drainage, the nonwetting phase invades the macropores before invading the microporous phase.

The volume of the microporosity acting in parallel to the macropore segments is assumed to be the same for each segment. It is given by

$$V_{\text{seg}} = F_{\text{mi}}\, V_{\text{img}} / N_{\text{seg}} = A_{\text{con}} l_{\text{con}}, \tag{11}$$

where N_{seg} is the number of segments and V_{img} is the volume of the 3D images ($F_{\text{mi}} V_{\text{img}}$ corresponds to the entire volume of the microporous phase). Supposing that the microporosity volume has a cuboid shape, we define A_{con} as the cross section of the cuboid perpendicular to the flow direction, whereas l_{con} corresponds to its length along the flow direction [see Fig. 7(b)].

The electrical conductance of the microporous phase $g_{e,\text{mi}}[S_{w,\text{mi}}\ (P_c)]$, depending on the water saturation of the microporous phase, is then given by

$$g_{e,\text{mi}}\left[S_{w,\text{mi}}(P_c)\right] = \sigma_w \{F_{f,\text{mi}} R_{\text{ind,mi}}[S_{w,\text{mi}}(P_c)]\}^{-1} A_{\text{con}}/l_{\text{con}}, \tag{12}$$

with $F_{f,\text{mi}} = a\varphi_{\text{mi}}^{-m_{\text{mi}}}$ and $R_{\text{ind,mi}}[S_{w,\text{mi}}(P_c)] = S_{w,\text{mi}}^{-n_{\text{mi}}}(P_c)$, where n_{mi} denotes the matrix saturation exponent and m_{mi} denotes the matrix cementation exponent. Obviously, the ratio $A_{\text{con}}\ /l_{\text{con}}$ strongly influences the conductance of the microporous phase. Electrical conductance of the solid phase was set to zero, as conductivity due to the small amount of submicropores in the solid phase is negligible in comparison to that of the macro- and micropores. Calcite itself, the principal component of carbonates, is not conductive.

E. Parameter determination for the dual network approach

Parameter determination of the dual network approach consists of two steps. In the first step, the microporosity properties are determined (microporosity fraction, mean porosity of the microporous phase, and fraction F_{surf} of the macroporosity surface in contact with microporosity). In the second step, the equivalent network of the macroporosity is built. The macroscopic properties of the microporosity are then added to this network, assuming that the micro- and macroporosity systems act in parallel.

The contact surface F_{surf} given in Table I is converted into a discrete number of macropore segments whose microporosity conductance is given by $g_{e,\text{mi}}$.. $g_{e,\text{mi}}$ of the remaining pore segments are set equal to zero, representing the solid phase (cf. Fig. 7). Pore segments with microporosity acting in parallel are randomly chosen. The percentage p_{seg} of these pore segments is then varied taking into account that the total volume of microporosity is constant. V_{seg} becomes then

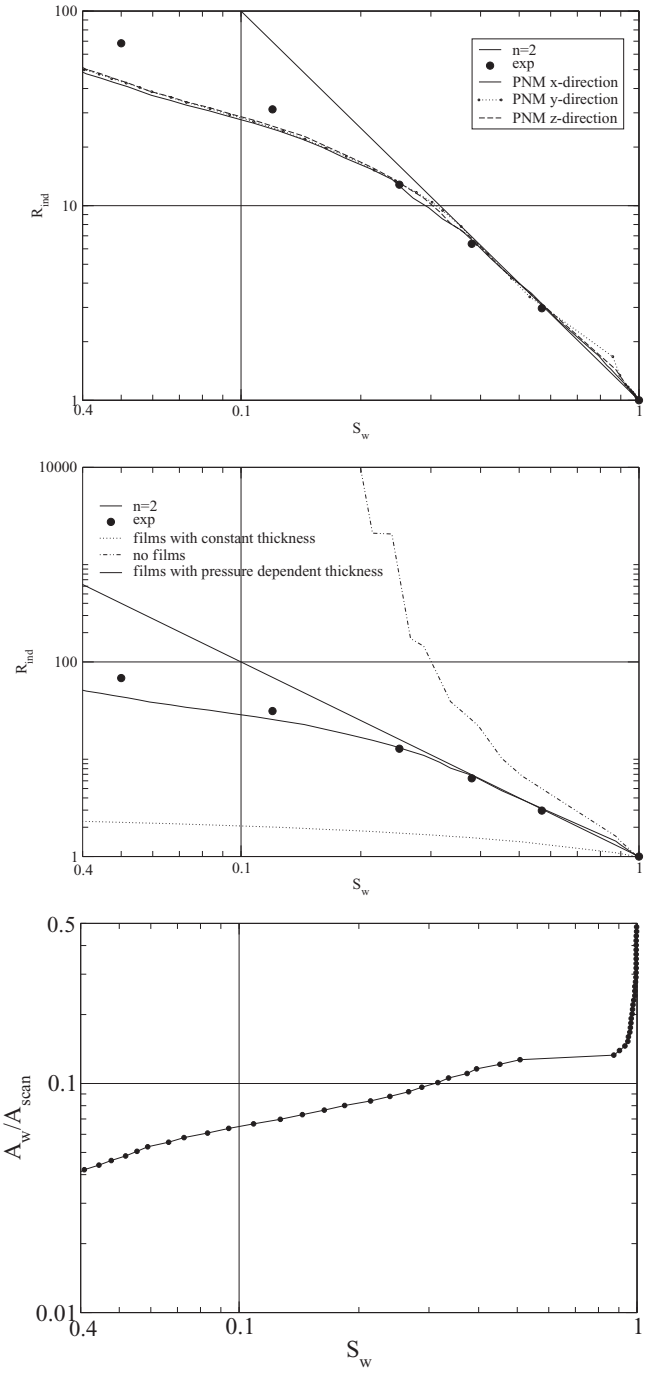

FIG. 8. (a) Resistivity index curves of the Fontainebleau sandstone: simulations and corresponding measurements, RI dimensionless, S_w percentage. (b) R_{ind} curves of the Fontainebleau sandstone for the following cases: no films, films of constant thickness, and films with pressure-dependent thickness, R_{ind} dimensionless, S_w percentage. (c) Ratio A_w/A_{scan} as a function of the water saturation, S_w percentage.

$V_{\text{seg}} = F_{\text{mi}}\ V_{\text{img}}\ /(p_{\text{seg}}\ N_{\text{seg}})$. The porosity of the microporous phase is deduced from the μ-CT measurement. If we assume that the microporosity consists mainly of packed calcite micrite, the cementation exponent m_{mi} can be set to $m_{\text{mi}} = 1.5$ [53,54].

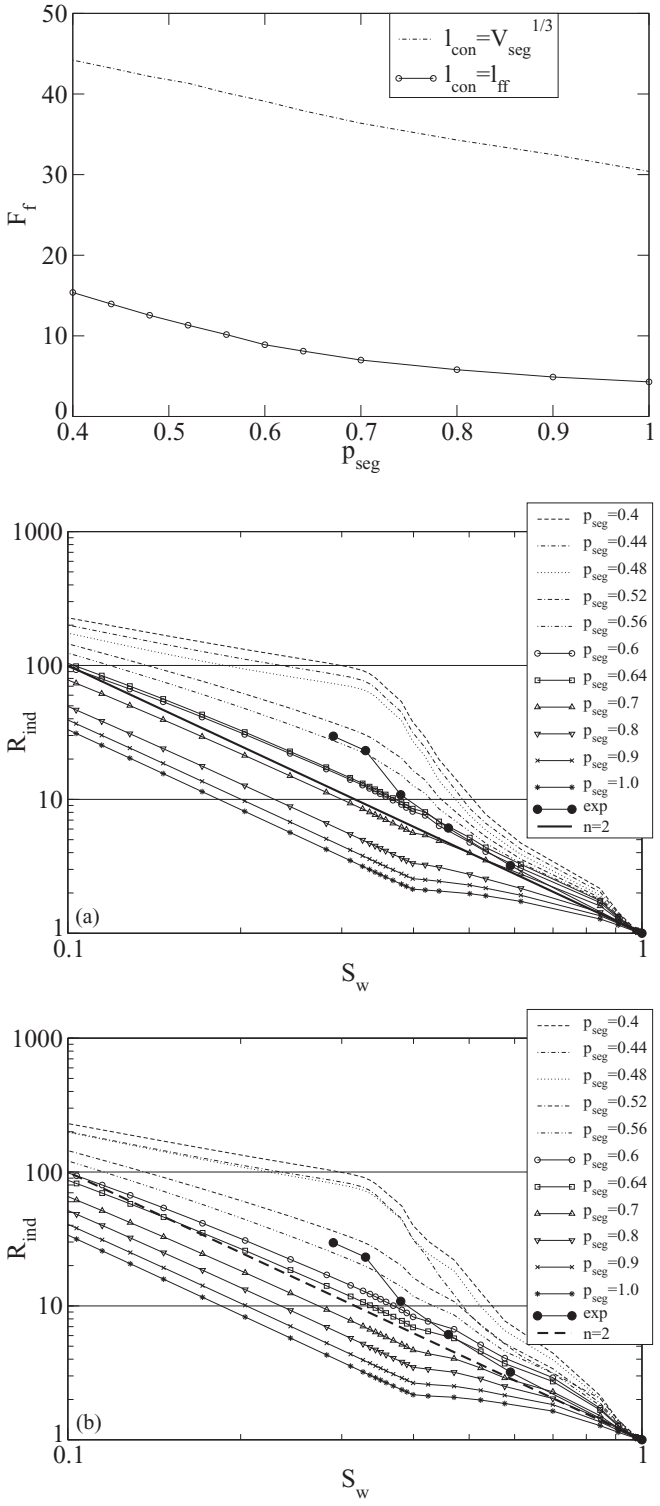

FIG. 9. (a) Estaillade carbonate: F_f as a function of the percentage of throats p_{seg} surrounded by microporosity for $l_{\text{con},i} = l_{\text{ff},i}$ and $l_{\text{con}} = V_{\text{seg}}^{1/3}$, F_f dimensionless. (b) Estaillade carbonate: R_{ind} as a function of the percentage of throats p_{seg} surrounded by microporosity [(a) $l_{\text{con},i} = l_{ff,i}$, (b) $l_{\text{con}} = V_{\text{seg}}^{1/3}$], RI dimensionless, S_w percentage.

The microporous phase saturation exponent was set to $n_{\text{mi}} = 2$ corresponding to the Archie exponent commonly used for homogeneous structures. The oil-water capillary pressure of the microporous phase $P_{c,\text{oil-water,mi}}$ was calculated from the mercury injection curve assuming that all pores that are smaller than the μ-CT resolution belong to the microporous phase.

V. RESULTS

In a first step, we show the numerical results (F_f, R_{ind}) of a monomodal porous medium (Fontainebleau sandstone) and compare them to experimental results. Then, the dual network approach is applied to an Estaillade and a Lavoux carbonate, and electrical properties are simulated.

A. Monomodal pore structure

Calculations were done using no-flow boundary conditions for the three spatial directions. F_f simulation results are compared to the experiment in Table II. Results are in good agreement with the experimental values, confirming the fact that geometrical network properties obtained from the segmented images enable the simulation of the correct transport behavior.

Figure 8(a) shows the resistivity index curve simulations as well as the experimental results. As can be seen, the numerically obtained saturation exponent decreases similarly to the experimental data, from 2 at high water saturation to a smaller value at low water saturation. Nevertheless, for low water saturation, R_{ind} values are slightly smaller than the experimental ones. In this range, as was already mentioned, the shape of the R_{ind} curve depends principally on the presence of water films. Thus, in the present work, the introduction of film conductance in the PNM simulations is critical for reproducing the experimentally observed bending-down deviation. Figure 8(b) shows R_{ind} curves for the following cases: no films, films of constant thickness, and films with pressure-dependent thickness. The strong increase in R_{ind} if no films are used is due to the gradual loss of continuity of the wetting phase. Identical results have been observed by Han *et al.* [10], Wang *et al.* [55], and Montaron [17]; to overcome this deficiency, Han *et al.* [10] proposed to use constant thick films with the size of a fraction of a micron given the fact that the average pore entry diameter is about 50 μm. Good results were obtained. The constant film size used for the PNM calculations shown in Fig. 8(b) is obtained from Eq. (8), where the radius ρ is taken as constant corresponding to the inverse of the lowest pressure necessary to invade at least one throat. As can be seen, the divergence of the R_{ind} curve is eliminated; however, the values are too low. Thus, the R_{ind} behavior depends strongly on the definition of a physically correct film thickness. This is done in PNM calculations by means of Eq. (8), directly introducing films with pressure-dependent thickness. In this case, we obtain results in good accordance with the experimental data. Figure 8(c) shows the ratio A_w/A_{scan} as a function of water saturation. Values

TABLE II. F_f values of the Fontainebleau sandstone, F_f dimensionless.

l_{ff}, A_{scan} no-flow boundary condition	measured F_f
10.16 (x), 9.65 (y), 10.71 (z)	11.5 ± 0.9

are slightly higher than those proposed by Han *et al.* [10], which explains the minor difference between the numerical and experimental values of R_{ind} for low water saturation. Thus, for low water saturation, Eq. (8) might be improved when using the numerical model for networks based on μ-CT imaging. However, in the following section on dual-porosity systems, we are principally interested in the high water saturation range. Thus, model equations will be used without modifications, as very good results were obtained in this saturation range.

B. Bimodal pore structure

As mentioned above, two distinct carbonates (Estaillade and Lavoux) were studied. The main objective of this section is to investigate the influence of the spatial distribution of the microporous and the solid phase on the macroscopic transport properties.

1. Estaillade carbonate

Figure 9(a) shows the results of the F_f calculation as a function of the percentage of throats surrounded by microporosity p_{seg}. Calculations were done for $l_{\mathrm{con}} = V_{\mathrm{seg}}^{1/3}$ ($l_{\mathrm{con}} = 56.25\ \mu$m if $p_{\mathrm{seg}} = 1$) assuming that the microporosity volume has a cubic structure, and for $l_{\mathrm{con,i}} = l_{ff,i}$ ($\langle l_{ff,i} \rangle = 11.0\ \mu$m), where $l_{ff,i}$ stands for the equivalent electrical length of a throat. As $l_{\mathrm{con},i} = l_{ff,i} < l_{\mathrm{con}} = V_{\mathrm{seg}}^{1/3}$, we have $g_{e,\mathrm{mi}}$ ($l_{\mathrm{con},i} = l_{ff,i}$) $> g_{e,\mathrm{mi}}$ ($l_{\mathrm{con}} = V_{\mathrm{seg}}^{1/3}$). The resulting formation factors are relatively close to the experimental value F_f =24. However, they become too high by using $l_{\mathrm{con}} = V_{\mathrm{seg}}^{1/3}$ and too low by using $l_{\mathrm{con},i} = l_{ff,i}$. This means that by correctly adapting the conductivity length of the microporosity l_{con}, the experimental value can be obtained. All values decrease with increasing p_{seg} as the number of percolating paths of microporosity volumes, and therefore the overall conductivity of the microporosity, increases.

Figure 9(b) shows the R_{ind} values as a function of p_{seg} for $l_{\mathrm{con},i} = l_{ff,i}$ and $l_{\mathrm{con}} = V_{\mathrm{seg}}^{1/3}$. R_{ind} values increase with decreasing p_{seg}, and for $p_{\mathrm{seg}} < p_{\mathrm{dc}}$, the formation of a double curvature can be seen. In both cases, the double curvature can be explained as follows. For high wetting phase saturation ($S_w \geqslant 0.4$), a percolating path in the macroporous phase still exists. For intermediate wetting phase saturation ($0.3 < S_w < 0.4$), the percolation of the wetting phase is either mostly provided by the microporous phase ($p_{\mathrm{seg}} > p_{\mathrm{dc}}$) or by the remaining water films lining the macropores ($p_{\mathrm{seg}} < p_{\mathrm{dc}}$). In the first case, the change in R_{ind} for a given change in wetting phase saturation ($\partial RI/\partial S_w$) is given by the electrical properties of the microporous phase. In the second case, the important change in the R_{ind} curvature results from the fact that there is no more percolating path in the microporous phase and the resistivity is dominated by the remaining water films in the macropores.

To illustrate this process, we investigated the percolation threshold of the macropore network more thoroughly. Figure 10 shows a small part of the studied volume in which only the macropore segments associated with microporosity have been represented for different p_{seg} [Fig. 10(a), $p_{\mathrm{seg}} = 1$; Fig. 10(b), $p_{\mathrm{seg}} = 0.5$; Fig. 10(c), $p_{\mathrm{seg}} = 0.4$]. Whereas for $p_{\mathrm{seg}} = 0.5$ a percolating microporosity path still exists, there is no more microporosity percolation for $p_{\mathrm{seg}} = 0.4$. Thus, the wetting phase conduction is only assured by the remaining water films, in this case leading to the experimentally observed double curvature in the R_{ind} curves.

As can be seen in Fig. 9(b), the numerical results for $l_{\mathrm{con}} = V_{\mathrm{seg}}^{1/3}$ for $p_{\mathrm{seg}} = 0.56$ are in relatively good agreement with the experimental results (black dots). We would also like to point out that $p_{\mathrm{seg}} = 0.56$ is very close to the measured contact surface F_{surf} obtained by the three-phase segmentation ($F_{\mathrm{surf}} = 47\%$, see Table I) corresponding to the percolation threshold of the microporosity, and therefore justifying by itself the experimentally observed double curvature.

In contrast, for $l_{\mathrm{con,i}} = l_{ff,i}$, although the double curvature exists, numerical R_{ind} values in the range of the experimental data do not show this behavior. Even though the system is close to the percolation threshold, R_{ind} curves for $p_{\mathrm{seg}} = 0.52$ and 0.56 are relatively straight. This can be explained by the large value of $g_{e,\mathrm{mi}}$ ($l_{\mathrm{con,i}} = l_{ff,i}$). In this case, a small number of macropores surrounded by microporosity is sufficient to maintain water conductance, and the formation of the double curvature is only observed for lower p_{seg}. However, once reaching a certain value of p_{seg},$\partial RI/\partial S_w$ becomes very large and only R_{ind} values higher than the experimental ones are observed. This is in agreement with the fact, already observed

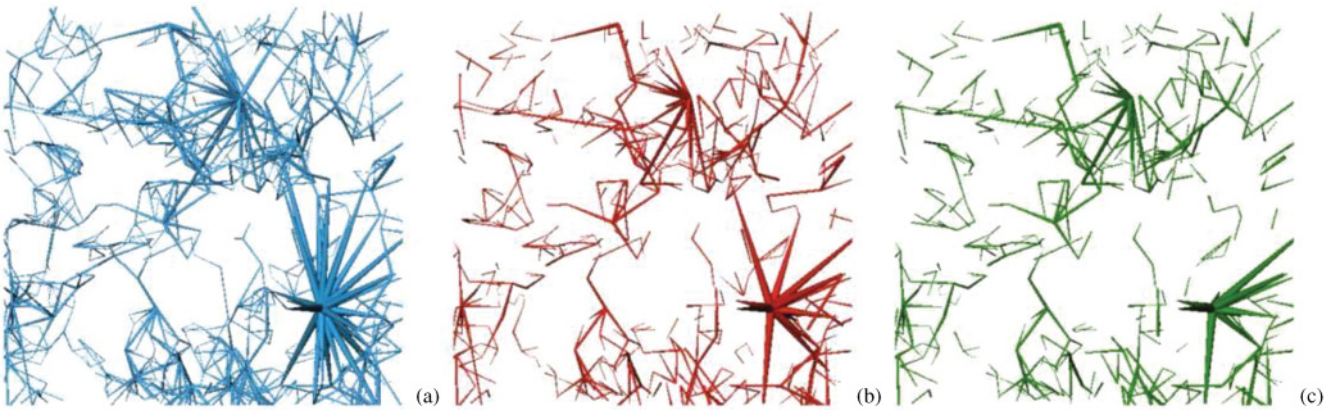

FIG. 10. (Color online) Estaillade carbonate: 3D representation of the segments associated with microporosity for different p_{seg} [(a) $p_{\mathrm{seg}} = 1$, (b) $p_{\mathrm{seg}} = 0.5$, (c) $p_{\mathrm{seg}} = 0.4$].

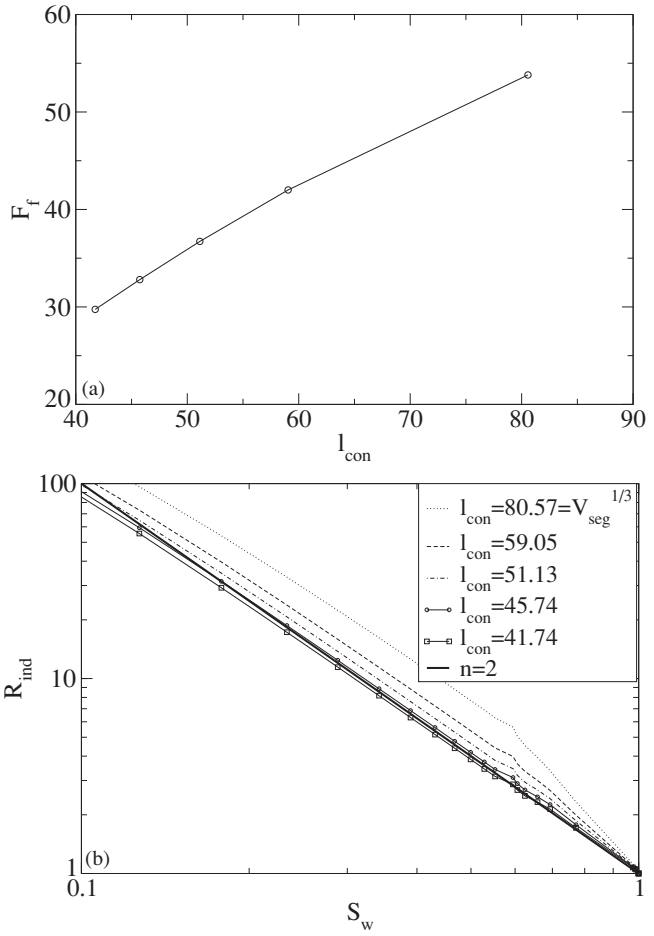

FIG. 11. Lavoux carbonate: F_f (a) and R_{ind} (b) as a function of l_{con} for $p_{\text{seg}} = 0.78$. F_f, dimensionless; R_{ind}, dimensionless; S_w, percentage; l_{con}, in microns.

for F_f, that the correct definition of l_{con} plays an important role.

2. *Lavoux carbonate*

The volume fraction of the microporous phase in the Lavoux sample is much higher than that of the Estaillade sample (about 60%), and the contact surface between macro and microporosity is $F_{\text{surf}} = 78\%$ (see Table I). As mentioned in Sec. II B, the R_{ind} curve does not show a double curvature; it follows Archie's law. This is due to the fact that the microporous phase is largely connected, which can be deduced from the high value of F_{surf}. As the microporosity fraction is very high in this sample, the important parameter to study is l_{con} rather than p_{seg}. Thus, the conductivity length l_{con} of the microporous volume of the Lavoux carbonate l_{con} was varied and p_{seg} fixed to 0.78. Figure 11 shows the F_f and R_{ind} calculations for different conductivity length l_{con}. As shown in this figure, by correctly describing l_{con}, the R_{ind} values fit well to the experimental results. However, with regard to F_f, calculated values shown in Fig. 11 are higher than the experimental value $F_f = 13$ (Fig. 1). On the one hand, this might be attributed to the heterogeneity of the Lavoux carbonate being relatively high in comparison to the sample size. On the other hand, it could probably be explained by the large range of throat sizes just below the μ-CT resolution, particularly in the range 1–3 μm (see the pore size distribution in Fig. 1). The conductivities of these pores are underestimated because they are taken into account as part of the microporous matrix assumed to be homogeneous. Indeed, as the present approach uses a homogeneous microporous matrix, it is best suited for bimodal structures where the throat size of the local minimum separating micro- and macroporosity (Fig. 1, mercury intrusion) is smaller than the μ-CT resolution (as in the Estaillade sample). Further improvements of the microporosity description are currently being considered.

VI. CONCLUSION

We present a general methodology to reproduce the electrical responses of monomodal and bimodal porous structures combining high-resolution μ-CT images with pore-network modeling. An equivalent pore network is built from 3D images, and the network parameters are extracted. For bimodal pore structures, a separate description of macroporosity and microporosity is given and the amount of macropore surfaces in contact with the microporous phase is determined, a useful quantity characterizing the link between these two pore systems. In the dual pore-network model, the microporosity is modeled as a parallel circuit located along the macropore throats and characterized by a conductivity length l_{con} and the fraction of throats (segments) p_{seg} in which microporosity is present.

Formation factors and resistivity indices of Fontainbleau sandstone and two very distinct carbonates were simulated and compared to measurements. The experimentally observed Archie behavior of the Lavoux carbonate, as well as the non-Archie behavior of the Fontainebleau sandstone and the Estaillade carbonate, was correctly reproduced, indicating that the model has the appropriate flexibility to reproduce different physical phenomena.

The experimentally obtained double curvature in the R_{ind} curves of Estaillade carbonate is often attributed to the heterogeneity of the sample. More deeply, by combining image analysis and pore-network modeling, we could show that the double curvature appears once the percolation threshold of the microporosity is reached. This percolation threshold is of the same order of magnitude as the contact surface between macro and microporosity F_{surf} measured on 3D images. It might, therefore, be interesting to verify this correlation between the double curvature and the value of F_{surf} in other carbonates.

Additionally, we have shown that simulation results depend on the parameter l_{con}, and we will focus in future work on its determination directly from μ-CT images.

Simulated F_f values of the Lavoux limestone are slightly higher than the experimental ones. This has been attributed either to the fact that the model is based on the hypothesis of a homogeneous microporous phase (not being the case for the Lavoux carbonate) or to the heterogeneity of the carbonate in comparison to the sample size. To confirm these assumptions, it would be interesting in future work to include the heterogeneity of the microporous phase into the model and to evaluate the influence of the sample size on the numerical results.

[1] G. E. Archie, Petrol. Trans. AIME **146**, 54 (1942).
[2] I. Schlumberger, *Log Interpretation Principles/Applications* (Schlumberger Educational Services, Houston, 1987).
[3] L. Bouvier and S. Maquignon, *Advances in Core Evaluation II: Reservoir Appraisal* (P. F. Worthington and D. Longeron, Gordon and Breach Science Publisher Ltd, London, 1991).
[4] M. Fleury, in *Proceedings of SPE/ATCE, San Antonio, 2002* (2002).
[5] J. W. Focke and D. Munn, SPE Formation Eval. **2**, 155 (1987).
[6] G. S. Padhy, M. A. Ioannidis, C. Lemaire, and M. Coniglio, in *Proceeding of the International Symposium of the Society of Core Analysts, Trondheim, Norway* (2006).
[7] M. Han, V. Tariel, S. Youssef, E. Rosenberg, M. Fleury, and P. Levitz, in *Proceedings of the SPWLA 49th Annual Logging Symposium, Edinburgh, Scotland* (2008).
[8] M. Han, Ec. Polytech., 2008.
[9] M. Han, M. Fleury, and P. Levitz, in *Proceeding of the International Symposium of the Society of Core Analysts, Calgary, Canada*, 34 (2007).
[10] M. Han, S. Youssef, E. Rosenberg, M. Fleury, and P. Levitz, Phys. Rev. E **79**, 031127 (2009).
[11] M. A. Knackstedt *et al.*, in *Proceeding of the International Symposium of the Society of Core Analysts, Calgary, Canada*, 33 (2007).
[12] M. Kumar, T. J. Senden, A. P. Sheppard, C. H. Arns, and M. A. Knackstedt, in *Proceedings of SPWLA 51th Annual Logging Symposium, Perth, Australia* (2010).
[13] H. N. Edmundson, Tech. Rev. **36**, 4 (1988).
[14] H. N. Edmundson, Tech. Rev. **36**, 12 (1988).
[15] M. A. Ioannidis, M. J. Kwiecien, and I. Chatzis, Transp. Porous Media **29**, 61 (1997).
[16] P. N. Sen, Geophysics **62**, 415 (1997).
[17] B. Montaron, Petrophysics **50**, 102 (2009).
[18] M. Sahimi, *Applications of Percolation Theory* (CRC, Boca Raton, FL, 1994), p. 276.
[19] S. Bekri, J. Howard, J. Muller, and P. M. Adler, Transp. Porous Media **51**, 41 (2003).
[20] T. W. Patzek and D. B. Silin, J. Colloid Interface Sci. **236**, 295 (2001).
[21] P. E. Oren, S. Bakke, and O. J. Arntzen, SPE J. **3**, 324 (1998).
[22] M. Piri and M. J. Blunt, Phys. Rev. E **70**, 061603 (2004).
[23] I. Fatt, Petrol. Trans. AIME **207**, 144 (1956).
[24] A. C. Payatakes, C. Tien, and R. M. Turian, AIChE J. **19**, 58 (1973).
[25] R. Lenormand, C. Zarcone, and A. Sarr, J. Fluid Mech. **135**, 337 (1983).
[26] C. E. Diaz, I. Chatzis, and F. A. L. Dullien, Transp. Porous Media **2**, 215 (1987).
[27] M. Blunt and P. King, Phys. Rev. A **42**, 4780 (1990).
[28] C. Laroche, O. Vizika, and F. Kalaydjian, J. Petrol. Sci. Eng. **24**, 155 (1999).
[29] A. I. M. Dicker and W. A. Bemelans, in *Proceedings of the SPWLA 25th Annual Logging Symposium, New Orleans* (1984).
[30] D. G. Zhou, S. Arbabi, and E. H. Stenby, Transp. Porous Media **29**, 85 (1997).
[31] Y. Wang and M. M. Sharma, in *Proceeding of the SPWLA 29th Annual Logging Symposium, San Antonio* (1988).
[32] M. M. Sharma, A. Garough, and H. F. Dunlap, Log Analyst **32**, 511 (1991).
[33] R. J. Suman and R. J. Knight, Geophysics **62**, 1151 (1997).
[34] H. N. Man and X. D. Jing, Transp. Porous Media **41**, 263 (2000).
[35] H. N. Man and X. D. Jing, J. Petrol. Sci. Eng. **33**, 101 (2002).
[36] C. D. Tsakiroglou and M. Fleury, Transp. Porous Media **35**, 89 (1999).
[37] M. A. Ioannidis and I. Chatzis, in *Proceedings of the International Symposium of the Society of Core Analysts, Abu Dhabi, United Arab Emirates* (2000).
[38] S. Bekri, C. Laroche, and O. Vizika, in *Proceedings of Computational Methods in Water Resources XIV, Delft, The Netherlands* (2002).
[39] S. Bekri, C. Laroche, and O. Vizika, in *Proceeding of the International Symposium of the Society of Core Analysts, Toronto* (2005).
[40] A. Moctezuma-Berthier, S. Bekri, C. Laroche, and O. Vizika, in *Proceeding of the International Symposium of the Society of Core Analysts, Pau, France* (2003).
[41] S. Youssef, M. Han, D. Bauer, E. Rosenberg, S. Bekri, M. Fleury, and O. Vizika, in *Proceedings of the International Symposium of the Society of Core Analysts, Abu Dhabi, UAE* (2008).
[42] D. A. Coker, S. Torquato, and J. H. Dunsmuir, J. Geophys. Res. Solid Earth **101**, 17497 (1996).
[43] P. Spanne, J. F. Thovert, C. J. Jacquin, W. B. Lindquist, K. W. Jones, and P. M. Adler, Phys. Rev. Lett. **73**, 2001 (1994).
[44] W. B. Lindquist, S. M. Lee, D. A. Coker, K. W. Jones, and P. Spanne, J. Geophys. Res. Solid Earth **101**, 8297 (1996).
[45] M. E. Coles, R. D. Hazlett, P. Spanne, E. L. Muegge, and M. J. Furr, SPE J. **1**, 295 (1996).
[46] F. M. Auzerais, J. Dunsmuir, B. B. Ferreol, N. Martys, J. Olson, T. S. Ramakrishnan, D. H. Rothman, and L. M. Schwartz, Geophys. Res. Lett. **23**, 705 (1996).
[47] S. Youssef, E. Rosenberg, N. Glan, S. Bekri, and O. Vizika, in *Proceeding of the International Symposium of the Society of Core Analysts, Calgary, Canada*, 17 (2007).
[48] O. Caty, E. Maire, S. Youssef, and R. Bouchet, Acta Mater. **56**, 5524 (2008).
[49] S. Youssef, E. Maire, and R. Gaertner, Acta Mater. **53**, 719 (2005).
[50] F. Cassot, F. Lauwers, and C. Fouard, Microcirculation **13**, 1 (2006).
[51] C. Laroche and O. Vizika, Transp. Porous Media **61**, 77 (2005).
[52] M. H. Hui and M. J. Blunt, J. Phys. Chem. B **104**, 3833 (2000).
[53] S. Bryant and N. Pallatt, J. Petrol. Sci. Eng. **15**, 169 (1996).
[54] P. N. Sen, C. Scala, and M. H. Cohen, Geophysics **46**, 781 (1981).
[55] K. W. Wang, J. M. Sun, J. T. Guan, and D. W. Zhu, Physica A **380**, 19 (2007).